7-2023

Analyzing the on Source Window of Supernova SN2019EJJ With a Multi Layered Signal Enhancement Algorithm With Coherent Waveburst and a Convolutional Neural Network

Michael Gale Benjamin
The University of Texas Rio Grande Valley

ANALYZING THE ON SOURCE WINDOW OF SUPERNOVA SN2019EJJ WITH A MULTI LAYERED SIGNAL ENHANCEMENT ALGORITHM WITH COHERENT WAVEBURST AND A CONVOLUTIONAL NEURAL NETWORK

A Thesis

by

MICHAEL BENJAMIN

Submitted in Partial Fulfillment of the

Requirements for the Degree of

MASTER OF SCIENCE

Major Subject: Physics

The University of Texas Rio Grande Valley

July 2023

ANALYZING THE ON SOURCE WINDOW OF SUPERNOVA SN2019EJJ WITH A MULTI LAYERED SIGNAL ENHANCEMENT ALGORITHM WITH COHERENT WAVEBURST AND A CONVOLUTIONAL NEURAL NETWORK

A Thesis
by
MICHAEL BENJAMIN

COMMITTEE MEMBERS

Dr. Soma Mukherjee
Chair of Committee

Dr. Malik Rakhmanov
Committee Member

Dr. Soumya D. Mohanty
Committee Member

July 2023

ABSTRACT

Benjamin, Michael, Analyzing the on source window of supernova SN2019ejj with a multi layered signal enhancement algorithm with coherent waveburst and a convolutional neural network. Master of Science (MS), July, 2023, 33 pp., 3 tables, 16 figures, references, 25 titles.

Core collapse supernovae (CCSN) are highly anticipated sources of gravitational waves during the fourth observation run (O4). CCSN signals are weak and unmodeled and the rate of occurrence in our galaxy is very low. Because of this, they provide a greater challenge to detect than previously detected GW sources. CCSN simulations are used to test the detection pipeline in the event a CCSN is detected. CCSN GW signals are often indistinguishable from the noise sources present in GW data. We present a multi layered signal enhancement pipeline which we have applied Machine Learning (ML) techniques. We have used a Convolutional Neural Network (CNN) to train on 10 different simulated CCSN signals, and then tested the preformance of our pipeline on rotating CCSN signals.

DEDICATION

Dedicated to my family, friends, my advisor and my colleagues to whom I could not do this without.

ACKNOWLEDGMENTS

We would like to acknowledge the LIGO-VIRGO-KAGRA (LVK) collaboration for use of their open source data, and the University of Texas Rio Grande Valley for their Teaching assistant position and the acceptance of the NSF S-STEM scholarship.

TABLE OF CONTENTS

Page

LIST OF TABLES

Page

LIST OF FIGURES

Page

CHAPTER I

INTRODUCTION

Gravitational waves were first detected in 2015 by the Laser Interferometer Gravitational wave Observatory (LIGO) [1], [9] . After this first detection won the Nobel prize in physics, gravitational wave astronomy has developed and is quickly developing into a major field in astrophysics with the introduction of multiple observatories, with the original two detectors in Hanford, Washington and Livingston, Louisiana. Currently, the gravitational wave detector network is made up of LIGO [9], VIRGO [8], and KAGRA [10]. Where VIRGO is the European gravitational wave detector network, and KAGRA is a Japanese detector that has recently opened, and will be added to the detector network soon.

In previous observation runs, LIGO has detected gravitational waves from two different sources, Binary black hole mergers, and Neutron star mergers. But as LIGO has started its fourth observation run and further, we hope to detect other sources of gravitational waves such as supernovae.

1.1 What are Gravitational Waves?

Gravitational waves are ripples in space-time caused by the motion of objects. Normally, these ripples are much too small to notice, but if an extremely violent and energetic event happens, I.E. a supernova, we can observe extremely minute ripples in space-time through an instrument called a laser interferometer. The laser interferometers used are laser arrays which are several kilometers across are built to precisely measure the distance between one end of the array and the other. When a gravitational wave passes through one of the beam arms (which is the name given to

the path the laser travels in the laser interferometer) it produces a extremely small variation in the distance between one end of the arm and the other. This variation is what we refer to as the strain, and using these extremely advanced interferometers, we are able to detect variations in strain as low as order of magnitude of 10^{-22}.

Gravitational waves are ripples in space-time caused by the motion of objects. Normally, these ripples in space-time are too small to notice or even detect but when a large and violent enough event with enough mass occurs, it can create large enough ripples in space-time that the distance that it changes can be observed with sensitive enough equipment

1.2 Previous major gravitational wave discoveries

The first official gravitational wave discovery happened in 2015, and was given the title GW150914 [1]. This signal was then proven to be a binary black hole merger, a binary system where two black holes orbit each other and as they orbit and draw closer to each other eventually merge. The second major GW discovery was the discovery of a second source of GW signals, which happened in 2017 and was given the title GW170817 [2]. This signal was the first binary neutron star in-spiral detected. It was also a major milestone as it was the first gravitational wave signal which was detected not just by gravitational wave detectors, but also verified by astronomers proving that LIGO can successfully detect events and have successfully detected events.

Since then, there have been hundreds of detections of both binary black hole mergers and binary neutron star in-spirals detected by the LIGO network. Going into the fourth observation (O4) run of LIGO, we expect to detect many more binaries, but the focus of this study, and the focus of our group is looking for a far more elusive source; supernovae.

1.3 the search for core collapse supernovae

Due to the higher sensitivity and larger areas of observation the fourth observation run has over the previous three, supernova are a highly anticipated source of Gravitational Wave detection. However, there are obstacles to overcome in the detection of supernova signals.

Firstly, our current detection range for gravitational waves from supernovae is on the galactic scale because supernova GW signals are much weaker than GW signals from mergers. Secondly, the rate of galactic supernovae is only one every 100 years or so, with the last galactic supernova happening in 1987 [12]. Thirdly, the current detector network is most sensitive at frequencies in which supernovae are not as sensitive, as stated on FIG 1.1.

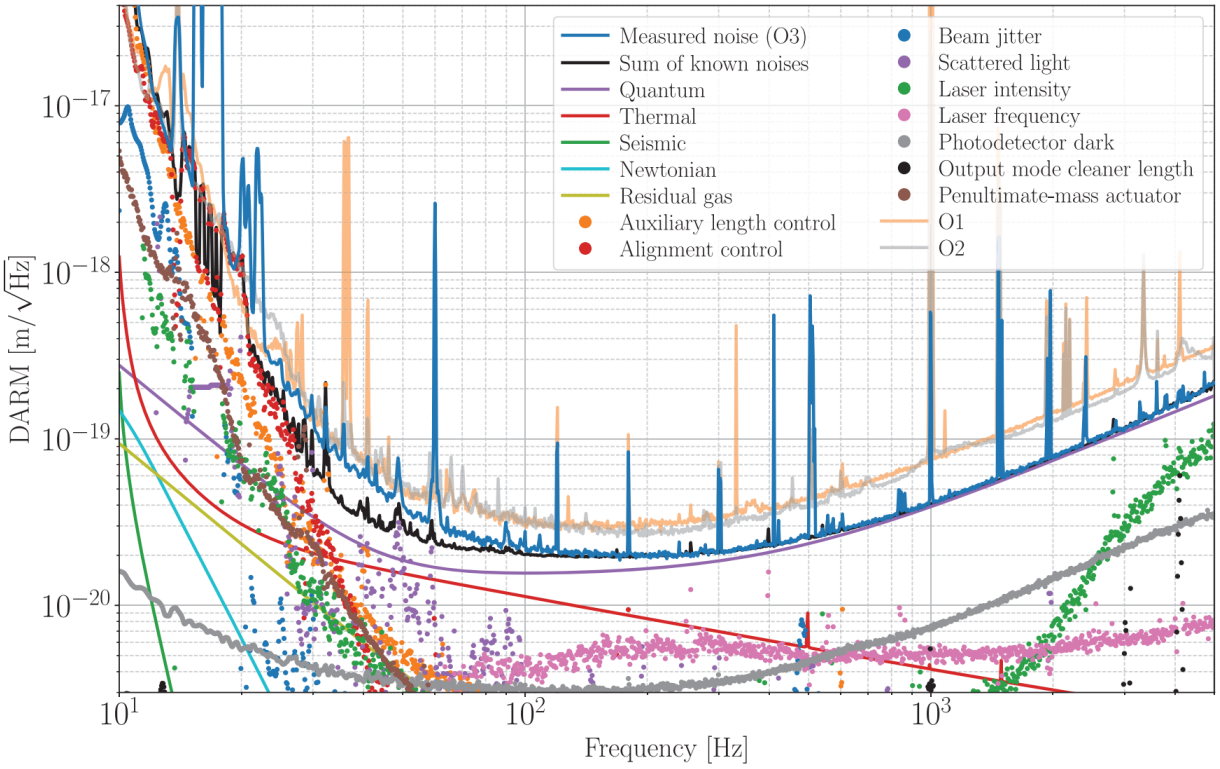

Figure 1.1: Above is the sensitivity curve for the Hanford observatory given for the third observation run (O3) [5].

CHAPTER II

CORE COLLAPSE SUPERNOVAE

2.1 CCSN explosion mechanism

A core collapse supernova, also known as Type II supernova is one of several possible endings for a star. These stars at the start of their life are primarily made up of hydrogen and helium, but throughout their life they start fusing the hydrogen and helium into heavier and heavier elements, until eventually the star fuses iron, which is the heaviest element the star can produce. This continues until the iron core reaches around 1.4 solar masses, at which point the core is too massive to supports its own weight, and collapses, beginning the "core collapse." [6].

The core collapse happens mechanism specifically occurs when the mass and temperature inside the core of the star causes photodisintegration [6], where photons have enough energy to destroy the the heavy iron nuclei built up in the core, and breaking them down into individual protons and neutrons, as described below from [6].

$$^{56}_{26}Fe + \gamma \rightarrow 13^{4}_{2}He + 4n \tag{2.1}$$

$$^{4}_{2}He + \gamma \rightarrow 2p^{+} + 2n \tag{2.2}$$

The conditions that exist once the iron core breaks down are extreme, and electrons are captured by the heavy nuclei and protons produced by the photodisintegration, as described by the equation below from [6]

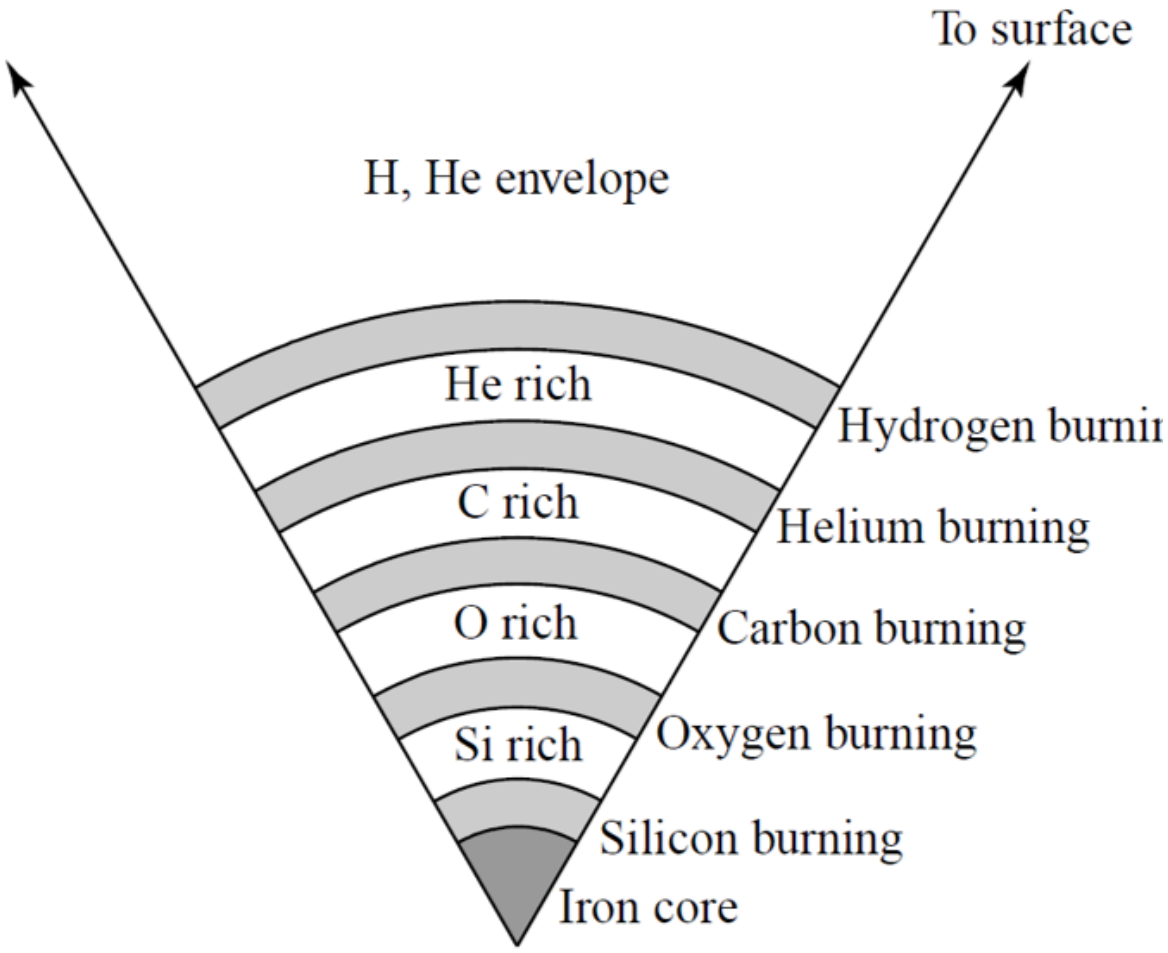

Figure 2.1: An example of the stages a star goes through in its lifetime [6], with the hydrogen and helium as an envelope, and as the hydrogen and helium slowly burn into carbon, then oxygen and then silicon, they eventually form an iron core, as iron is the heaviest element that can be formed through nuclear fusion.

$$p^+ + e^- \rightarrow n + \nu_e \tag{2.3}$$

The core collapse happens in a matter of seconds, as the iron core of the star falls in on itself and becomes so dense that the pressure within the star is comparable to the pressure within an atomic nucleus. This is the stage when the supernova emits gravitational waves, as the core collapse is so violent that the in-falling of the matter causes a large emission of energy [6].

2.2 what are the existing waveform models?

Because supernovae are unmodeled, and waveform models do not exist to accurately describe the supernova mechanisms yet. Because of this, there is a large community of supernova simulation groups who are developing simulations to better understand the supernova explosion mechanism. The LIGO supernova group put together a series of waveforms that give a rough estimation of how these preform when injected into the current pipeline [23], and the analysis of the waveforms and their properties are displayed on Table 1 of [23]. In these input waveforms, there are a range of different parameters that define a simulation such as the mass of the progenitor star, if it is rotating or not and how fast the star is rotating, the emitted gravitational wave energy, and the peak frequency.

CHAPTER III

DATA USED IN THE STUDY

3.1 what period of LIGO data is used

When we were training our Neural Network, we needed to choose a length of time to inject our supernova waveforms into. For this study, we used a length of data and a 3 day time window that corresponds to Supernova SN2019ejj. We chose this as the LIGO Supernova group has a currently accepted list of On Source Windows (OSWs) that, in the event of an actual supernova detection there is a window of time to look back from the first detection of supernova in order to constrain the search for the gravitational wave component of the signal.

The On Source Window mentioned in the previous paragraph is a term given by LIGO used in the detection of gravitational wave transients as described by [25] as a window of time which we constrain our search. The window of time is something that is given by a methodology which decides what the time window is, and the methodology gives the window based on the type of transient, and for supernovae it is given based on the optical and neutrino observations.

The LIGO Supernova group has chosen the OSWs of 8 supernova as optical targets for the third GW observation run and onwards, and SN2019ejj was one of them, and is the one we chose for this trial. Supernova SN2019ejj lasted from April 26th 2019 to April 29th 2019. The GPS times for this window are from 1240296814 to 1240553941 [25].

3.2 what CCSN models are used

17 supernova simulations were selected to train our supernova simulations, along with a set of background data used as a control. They were chosen to be as wide a range of data as possible as

to most broadly train our neural network. The waveforms we used to train our data are shown on table 3.1

Table 3.1: These are the waveforms used to train our neural network, The Waveform Family indicates which author and set of waveforms the simulations are organized into. The Numerical Method column dictates which simulation code was used to generate waveforms in the family. The GW Features list any identifiable features that are observed by the GW. The Waveform identifier lists the specific waveforms from the family. M_{star} gives the mass of each of the progenitor stars for each simulation, given in solar mass. Ω_c indicates if the supernova is rotating and how fast, with units in radians per second. f_{peak} indicates the peak frequency. E_{GW} gives the emitted energy of the supernova by gravitational wave emission, and the duration is the duration of the simulation given in milliseconds.

Waveform Family	GW Features	Waveform Identifier	$M_{star}[M_\odot]$	Ω_c [rad/s]	f_{peak} [Hz]	$E_{GW}[M_\odot c^2]$	Duration [ms]
Andresen 2016 [3]	g-mode SASI	s20	20	0	687	7.4×10^{-10}	430
Andresen 2019 [4]	g-mode SASI	s15nr	15	0	820	1.5×10^{-10}	350
		s15fr	15	0.5	689	2.7×10^{-10}	460
		s15r	15	0.2	801	7.1×10^{-11}	380
Cedra Duran 2013 [7]	BH formation g-mode SASI	fiducial	35	2.0	922	3.3×10^{-7}	1620
Kuroda 2016 [13]	g-mode SASI	TM1	15	0	714	1.7×10^{-9}	350
		SFHx	15	0	718	2.1×10^{-9}	350
Mezzacappa 2020 [15]	f-, g-, p-mode SASI	C15-3D	15	0	1064	6.4×10^{-9}	420
Morozova 2018 [16]	f-, g-, p-mode SASI	M10_DD2	10	0	1544	1.7×10^{-9}	1700
OConnor 2018 [19]	g-mode SASI	mesa20	20	0	1121	6.3×10^{-10}	500
Powell 2018 [20]	g-mode	s18	18	0	872	1.6×10^{-8}	890
Radice 2019 [22]	f-, g-mode SASI prompt-convection	s13	13	0	1422	5.9×10^{-9}	800
		s25	25	0	1132	2.8×10^{-8}	600
Richers 2017	bounce prompt-convection	A300w0.50_ HSDD2					

Once the CNN was trained, it was then used on a list of waveforms to test its performance. The list of waveforms used for analysis was largely the same as the one for training, but with a few key differences which are discussed in the caption of table 3.2.

Table 3.2: Displayed above are the waveforms used for testing, the data is largely the same, except for the omission of the Morozova 2018 DD2 waveform, and the Radice 2019 s25 waveform. We also added the Andresen 2016 s27, Mezzacappa 2022 D15-3D, Powell 2020 m39, and Radice 2019 s13 waveforms.

Waveform Family	GW Features	Waveform Identifier	$M_{star}[M_\odot]$	Ω_c [rad/s]	f_{peak} [Hz]	$E_{GW}[M_\odot c^2]$	Duration [ms]
Andresen 2016 [3]	g-mode SASI Convection	s20	20	0	687	7.4×10^{-10}	430
		27	27	0	753	4.4×10^{-10}	570
Andresen 2019 [4]	g-mode SASI	s15nr	15	0	820	1.5×10^{-10}	350
		s15fr	15	0.5	689	2.7×10^{-10}	460
		s15r	15	0.2	801	7.1×10^{-11}	380
Cedra Duran 2013 [7]	BH formation g-mode SASI	fiducial	35	2.0	922	3.3×10^{-7}	1620
Kuroda 2016 [13]	g-mode SASI	TM1	15	0	714	1.7×10^{-9}	350
		SFHx	15	0	718	2.1×10^{-9}	350 [c]
Mezzacappa 2020 [15]	f-, g-, p-mode SASI	C15-3D	15	0	1064	6.4×10^{-9}	420
Mezzacappa 2022 [14]		D15-3D					
OConnor 2018 [19]	g-mode SASI	mesa20	20	0	1121	6.3×10^{-10}	500
Powell 2018 [20]	g-mode	s18	18	0	872	1.6×10^{-8}	890
Powell 2020 [21]		m39					
Radice 2019	f-, g-mode SASI prompt-convection	s9	9	0	727	1.6×10^{-10}	1100
		s13	13	0	1422	5.9×10^{-9}	800
Richers 2017	bounce prompt-convection	A300w0.50_ HSDD2	12	0.5	701		1000

In the following chapter, we will give the explanation of what the convolutional neural network, and how it was used explicitly, along with a description of our pipeline.

CHAPTER IV

METHODS USED IN THIS STUDY

In previous sections, we gave a background of the field, and a description of what data we used, along with the motivation for said data. In this chapter we will discuss the methods of the pipeline which we are studying.

4.1 MuLaSEcC pipeline

The Multi Layered Signal Enhancement with coherent waveburst and a Convolutional Neural Network, as the title of this thesis suggests, is a multi-layered signal enhancement pipeline, with a convolutional neural network component which is then used on the coherent waveburst pipeline. The workflow this pipeline goes through is given by fig. 4.1.

The first step of the process is to train the neural network. which is represented on the left half of fig. 4.1, which then produces a confusion matrix, which is a representation of the preformance of the neural network. Once the neural network is trained, After this, we go through the right side of fig. 4.1 in order to produce efficiency curves, or coherent event displays (CED), which is a mode of cWB that produces the reconstructed waveform of a single event that was injected.

4.2 Description of MuLaSE

The MuLaSE module [18], [17] module of the pipeline is concerned with the whitening and signal enhancement. The methods used in the signal enhancement and denoising are discussed in [18] [17] but is reiterated here.

First, we assume an additive noise model, as introduced by the previously cited paper, as defined below

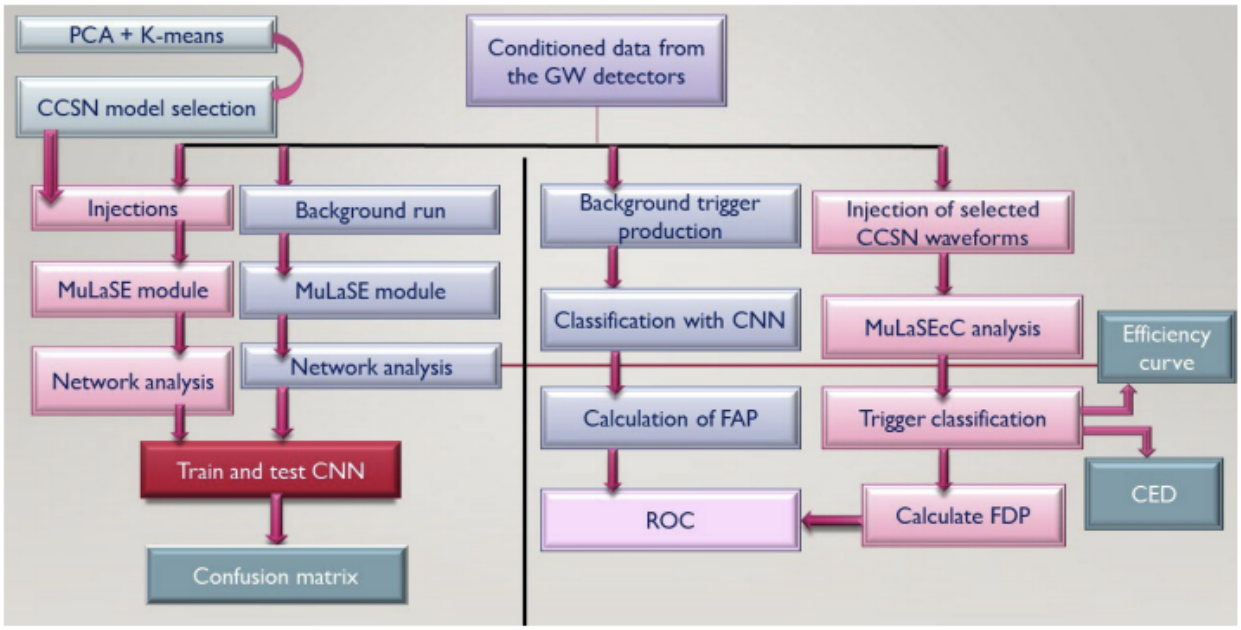

Figure 4.1: A flowchart of the MuLaSEcC analysis pipeline. The chart shows the three modular components of the pipeline, the left side of the figure dictates the component of the pipeline dedicated to training the CNN. While the right side of the flowchart is dedicated to the analysis, and application of the CNN.

$$x_p(t) = s_p(t) + n_p(t) \tag{4.1}$$

Where $x_p(t)$ is the output from the interferometers, $s_p(t)$ is the desired signal, and $n_p(t)$ is the noise. This signal then gets transformed into the frequency domain by fourier transform, which also transforms the signal and noise as denoted below.

$$X(p,k) = S(p,k) + N(p,k) \tag{4.2}$$

Where $X(p,k)$, $S(p,k)$, and $N(p,k)$ are the data, signal and noise in the frequency domain respectively. We then take the power spectral density of our additive noise model as shown below,

$$P_{XX}(p,k) = P_{SS}(p,k) + P_{NN}(p,k) \tag{4.3}$$

An estimate of the signal $\widehat{S}(p,k)$ is then what we are looking for, which is a function of

the input data, and the PSDs of the noise and signal. The estimated signal can be defined as some function of the previously introduced below.

$$\widehat{S}(p,k) = f(P_{NN}(p,k), P_{SS}(p,k), x(p,k)) \tag{4.4}$$

This function was found to be a spectral gain $\Gamma(p,k)$, which requires an estimate of the signal to noise ratio (SNR), which [18] cites the definition as shown below, where $\tilde{s}(f)$ is the fourier transform of the GW signal, and $N(f)$ is the one sided PSD of the noise.

$$snr = [4\int_0^\infty df \frac{|\tilde{s}(f)|^2}{N(f)}]^{\frac{1}{2}} \tag{4.5}$$

From this, two parameters are introduced for the purposes of defining in our spectral gain,

$$snr_{post}(p,k) = \frac{|X(p,k)|^2}{P_{NN}(p,k)} \tag{4.6}$$

$$snr_{priori}(p,k) = \frac{P_{SS}(p,k)}{P_{NN}(p,k)} \tag{4.7}$$

Using these definitions of $snr_{post}(p,k)$ and $snr_{priori}(p,k)$, we have the form of the spectral gain $\Gamma(p,k) = f(\widehat{snr}_{priori}(p,k), \widehat{snr}_{post}(p,k))$. This gives a function more defined to estimate a signal below,

$$\hat{S}(p,k) = \Gamma(p,k)X(p,k) \tag{4.8}$$

Mukherjee and Salazar then proceeds to find $\Gamma(p,k)$ by defining a relation between the $SNR_{post}(p,k)$ and $SNR_{priori}(p,k)$, which is first done by defining the amplitude of the data of the data stream as a function of the signal and noise. And then by defining the local versions of the two SNR values.

$$|X(p,k)| = \sqrt{|S(p,k)|^2 + |N(p,k)|^2 + 2|S(p,k)||N(p,k)|\cos\beta(p,k)} \tag{4.9}$$

And then the definition of the posteriori snr.

$$snr_{post}^{local}(p,k) = \frac{|X(p,k)|^2}{|N(p,k)|^2} \tag{4.10}$$

followed by the priori snr.

$$snr_{priori}^{local}(p,k) = \frac{|S(p,k)|^2}{|N(p,k)|^2} \tag{4.11}$$

Then by combining the amplitude of the data stream as a function of the local SNR, they get the following equation.

$$snr_{post}^{local}(p,k) = 1 + snr_{priori}^{local}(p,k) + 2\cos\beta(p,k)\sqrt{snr_{priori}^{local}(p,k)} \tag{4.12}$$

They then introduce an estimator called the 'decision directed' (DD) approach, which combines the amplitude of the previous time frame and the current time frame of the data stream. They then define the decision directed priori snr snr_{priori}^{DD} below.

$$snr_{priori}^{DD}(p,k) = \varepsilon\frac{|S(p-1,k)|^2}{P_{NN}(p,k)} + (1-\varepsilon)P[snr_{post}(p,k)-1] \tag{4.13}$$

Where $P[.]$ is the half wave rectification which cuts off negative values with the following properties

$$P[x] = x\ if\ x \geq 0 P[x] = 0\ else \tag{4.14}$$

And then with this description, the decision directed spectral gain is defined as such.

$$\Gamma_{DD}(p,k) = \frac{snr_{priori}^{DD}(p,k)}{1 + snr_{priori}^{DD}(p,k)} \tag{4.15}$$

Finally, Mukherjee and Salazar use the decision directed snr to define the two step denoising snr or two step noise reduction (TSRNR), which not only calculates the snr from the current and

previous time frames, but also adds the following (the $(p+1)$th time frame), as described below.

$$snr^{TSNR}_{priori}(p,k) = snr^{DD}_{priori}(p+1,k) \tag{4.16}$$

And then the TSNR spectral gain was defined as such,

$$\Gamma_{TSNR}(p,k) = \frac{snr^{TSNR}_{priori}(p,k)}{1+snr^{TSNR}_{priori}(p,k)} \tag{4.17}$$

Which is how the signal is estimated using the two step noise reduction.

4.3 description of Convolutional Neural Network

The Convolutional Neural Network (CNN) used in this study as described by figure 4.2 works by breaking down images provided to it into matrices, and convolves the matrices in multiple layers, which then leads to features in images being identified by the neural network. The advantage of a CNN is that it can be trained to recognize visual shapes or patterns on a large scale, such as the shape of a number or a letter to identify text from handwriting, or to identify particular objects in an image. This is advantageous for us, as supernovae have distinct features that appear in time frequency spectrograms, and are what lets a researcher looking at a spectrogram identify themselves if they are looking at a spectrogram or just noise.

We prepared our training data in several steps. First, we use cWB to inject waveforms, and save spectrograms of what it reconstructs as events. At this stage, cWB has not yet determined if what it is looking at is a glitch or a real GW event, but due to the high SNR values we inject our simulations at, the spectrograms are always clearly supernova injections. Once the reconstructed spectrograms are produced, they are than cropped and down-scaled to remove axis labels, to center on the event itself, and to reduce the amount of time the training takes.

The first step in the analysis is reading raw strain data from the LIGO Hanford (H1) and LIGO Livingston (L1). Next, conditioning the data by band-passing to remove the seismic noise in lower frequencies and shot noise in higher frequencies, and then to re-sample the data down to

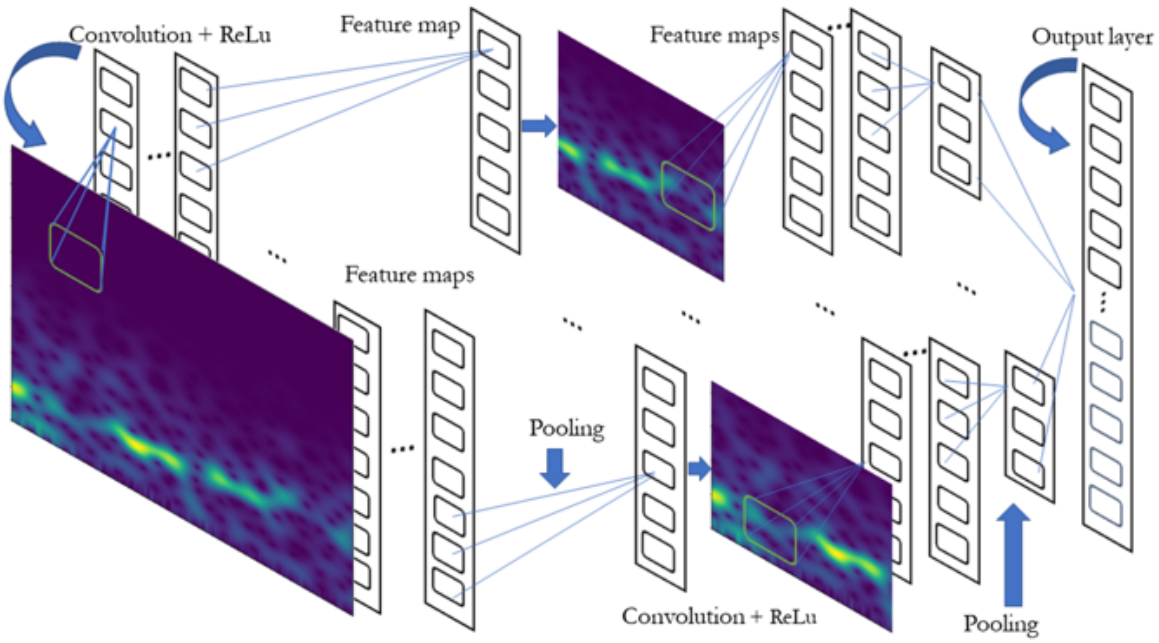

Figure 4.2: An example of how the CNN arcitecture is trained on gravitational wave data in the spectrogram form, as produced by S. Mukherjee, G. Nurbek, and O. Valdez [17]

2048 Hz. After this, the data is whitened to remove narrow band noise. Once this conditioning has taken place, it then enters the modular mulase component of the analysis, where a statistically educated estimate of signals embedded in the data are processed. The output from mulase is then applied as input to the network analysis which generates a large number of background glitches as output. Each background glitch is then recorded and converted into a time-frequency image. The next part of the analysis occurs when selected CCSN waveforms are injected into noise from the detector during the time window given during O3a in this study. As described in section III, waveforms are selected to maximize their representative features of the CCSN waveform landscape. The analysis at this stage follows a similar one to that done for the background, with the difference being that the output is a set of CCSN signals that have been injected into the LIGO O3 noise. The CNN is then trained on the background glitches along with the data with the injected CCSN signals that have been detected from the injections. Once the CNN has been trained, a new test set of data is created to measure the preformance of it using the triggers produced in the data.

The next part of the analysis demonstrates the network analysis. First starting with the data streams from the detectors with injected signals, and then following the MuLaSEcC steps of the analysis pipeline similar to the description in the preceding paragraph. The network analysis ends with the production of detected events. At this stage, the output triggers are subjected to classification and are trained by the CNN. The classification enables selection of the CCSN signals and rejection of the noise. Then efficiency curves are created as either a function of distance or SNR.

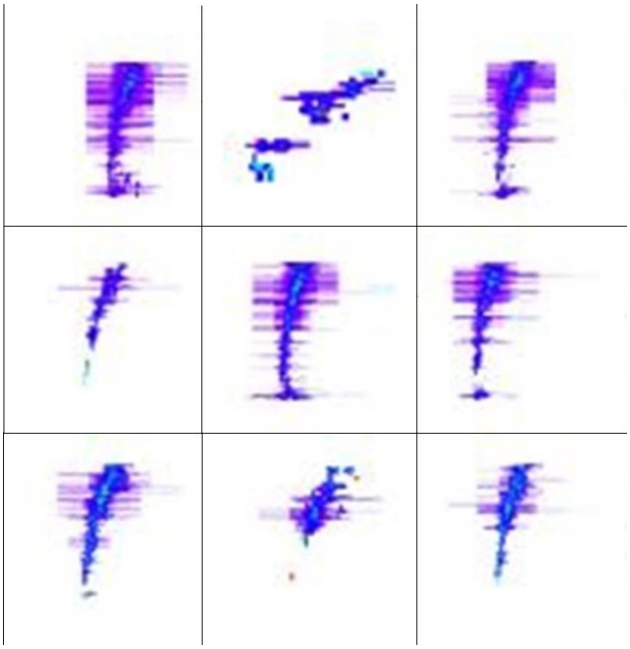

Figure 4.3: A 3x3 grid of example spectrograms that were used to train our CNN. These are reconstructions of the Powell 2018 - s18 waveform.

4.4 Description of cWB

The methodology of how coherent waveburst (cWB) is developed in [11]. The cWB algorithm works by first taking the data stream from the detectors and putting them through a discrete wavelet transformation (DWT) to break down the data stream into the time-frequency domain. After which, a black pixel probability cluster selection is preformed, and then a constrained likelihood function is preformed on the decomposed data. After all of this, the inverse of the wavelet transformation is computed to result in an estimated signal. A visual description of this process is

given by fig. 4.4.

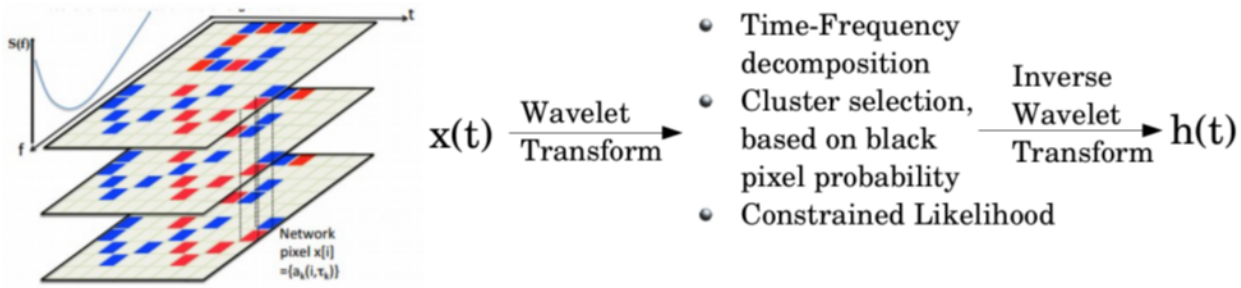

Figure 4.4: The figure here by M. Szezepanczyk [24] describes the cWB pipeline, where the data stream from the detectors $x(t)$ is sent through a wavelet transformation in order to preform a time frequency decomposition of the data, a cluster selection to determine data clustered in the time-frequency plane, and then a constrained likelihood function to determine the likelihood of the clusters being signals or noise. After which, an inverse wavelet transform is preformed to result in the estimated signal $h(t)$.

CHAPTER V

RESULTS

5.1 Analysis waveforms

The waveforms analyzed are listed in table 3.2. Below, we show all of the SNR efficiency curves produced by both cWB and MuLaSEcC. The efficiency curves produced plot injected SNR values on the x-axis, and the probability of detection on the y-axis. We describe the efficiency curve as a representation of how likely it is that MuLaSEcC would detect a certain signal. With the distance or SNR axis being the strength of the signal being injected into data.

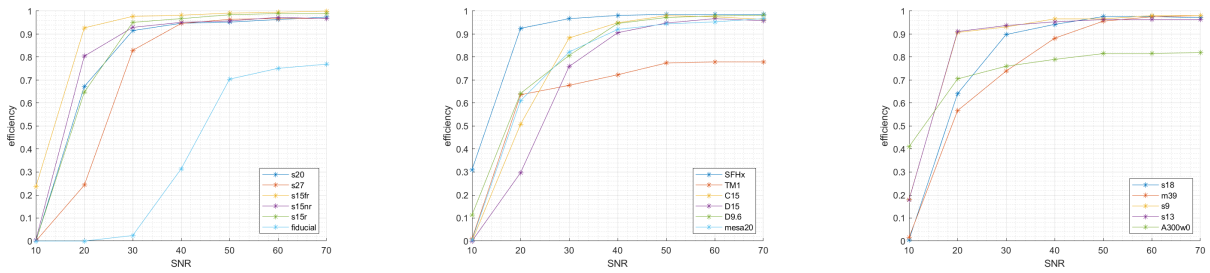

Figure 5.1: Given here are all of the waveforms efficiencies produced by cWB.

Next, we show all of the efficiencies in SNR produced by MuLaSEcC.

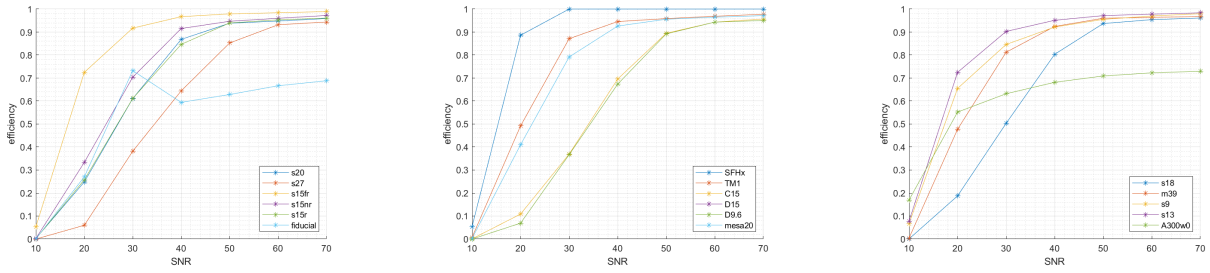

Figure 5.2: Given here are all of the waveforms efficiencies produced by MuLaSEcC.

5.2 Individual waveform analysis

Each of the waveforms mentioned in table 3.2 are discussed by directly comparing the efficiency curve produced by cWB. For the sake of brevity, we chose four out of the eleven waveforms to individually display from figures 5.1 and 5.2. We also show the receiver operating curves for each waveform, and discuss the importance of the results.

5.2.1 Efficiency curves

This section is focused on the individual efficiency curves, for Cedra-Duran 2013 fiducial, Kuroda 2016 as they preformed the best out of the analysis set of waveforms, and Mezzacappa 2020 C15-3D and 2022 D15-3D as they are the most complex waveforms produced to date.

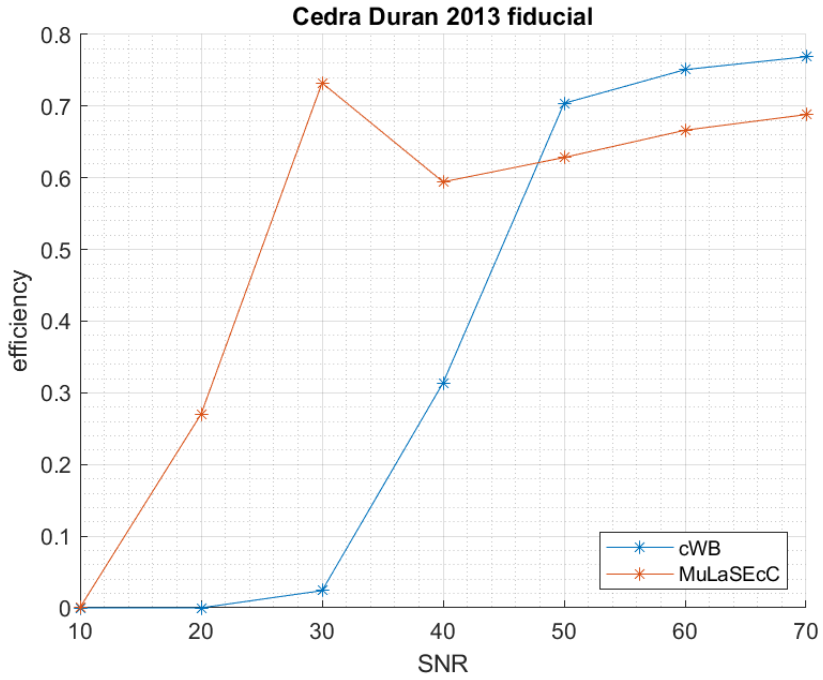

Figure 5.3: This figure shows the efficiency as a function of SNR for the Cedra-Duran 2013 fiducial waveform. the 50% efficiency for the cWB pipeline was found to be at SNR = 45, whereas the same for MuLaSEcC is at SNR = 28, indicating a more efficient performance.

After this, we show the reciever operating curves for each of these four waveforms.

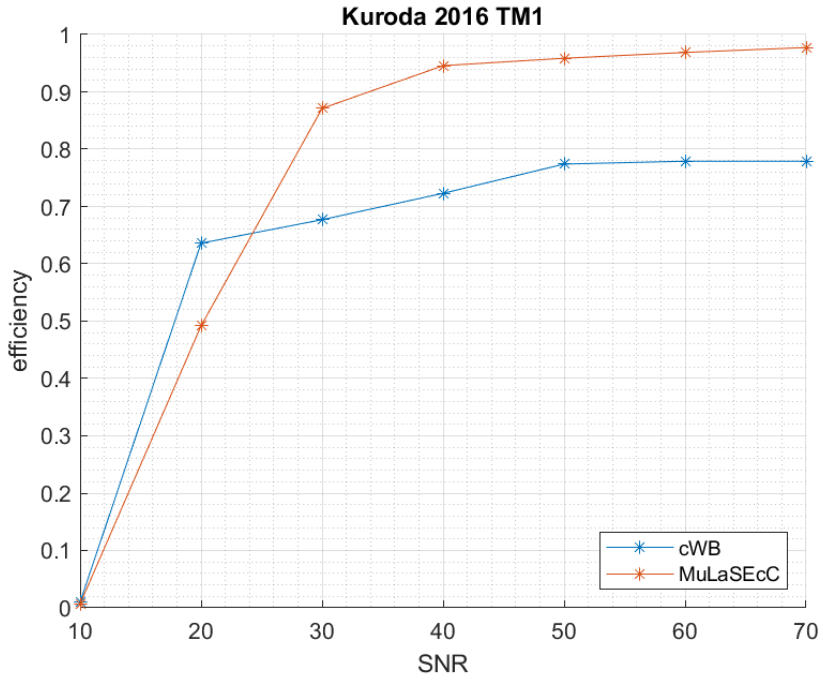

Figure 5.4: This figure shows the efficiency as a function of SNR for the Kuroda 2016 TM1 waveform. The 50% efficiency for the cWB pipeline was found to be between SNR = 10 and SNR = 20, and the same efficiency for MuLaSEcC is at 20% indicating a higher preformance.

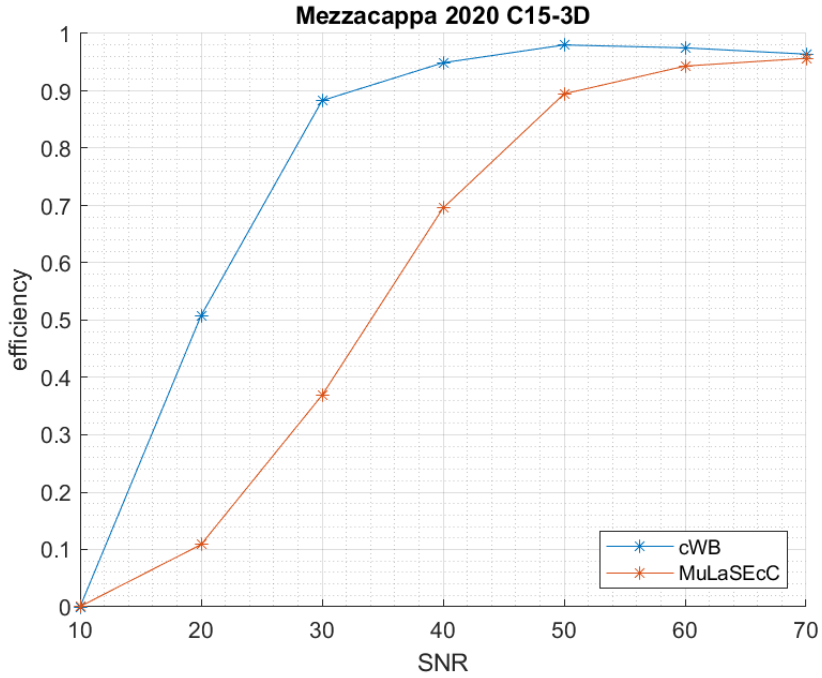

Figure 5.5: The above figure shows the efficiency as a function of SNR for the Mezzacappa 2020 C15-3D waveform. the 50% efficiency for the cWB pipeline is shown here to be at roughly SNR = 20, and the same is shown for MuLaSEcC to be at roughly SNR = 35, which shows that MuLaSEcC preforms poorly for this particular model.

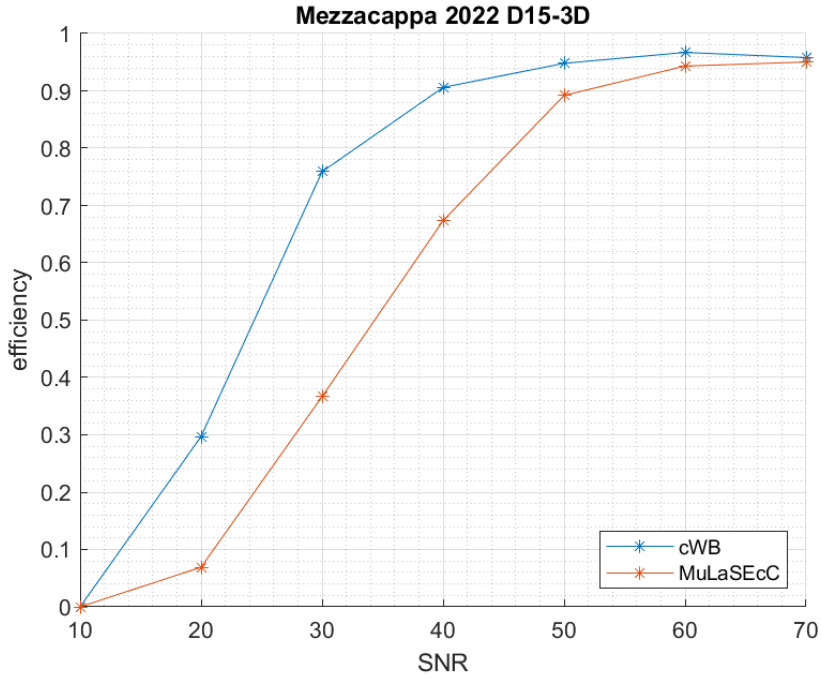

Figure 5.6: Above is the SNR efficiency curve for Mezzacappa D15-3D

5.2.2 Reciever Operating Curves (ROC)

This section shows the Reciever Operating Curves (ROC), which plot the inverse false alarm rate (iFAR) vs. the Detection Probability, which is meant to correlate how likely a signal is vs the probability of detecting a signal.

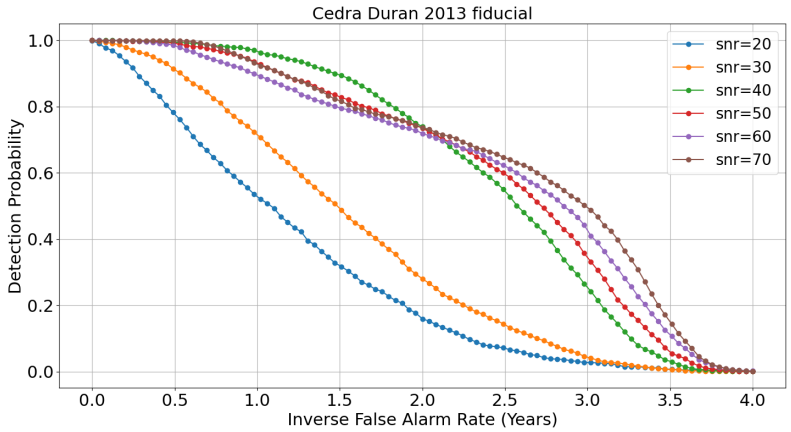

Figure 5.7: Above is the receiver operating curve for Cedra Duran 2013 fiducial. With increasing injection SNR, the 50% probability is acheived for higher iFAR.

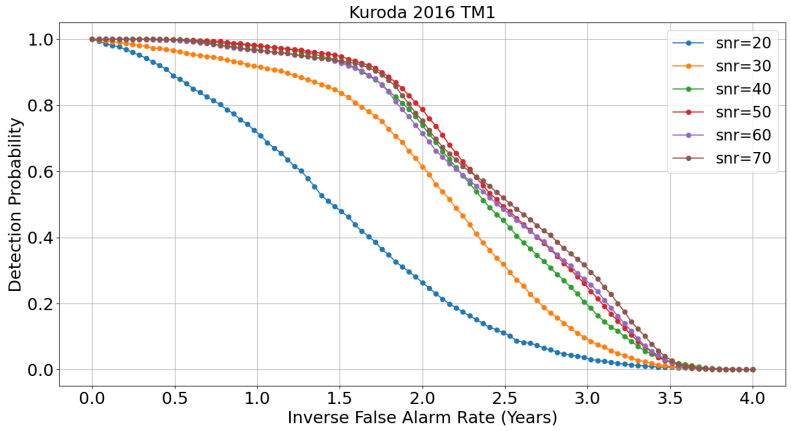

Figure 5.8: Above is the receiver operating curve for Kuroda 2016 TM1. With increasing injection SNR, the 50% probability is acheived for higher iFAR.

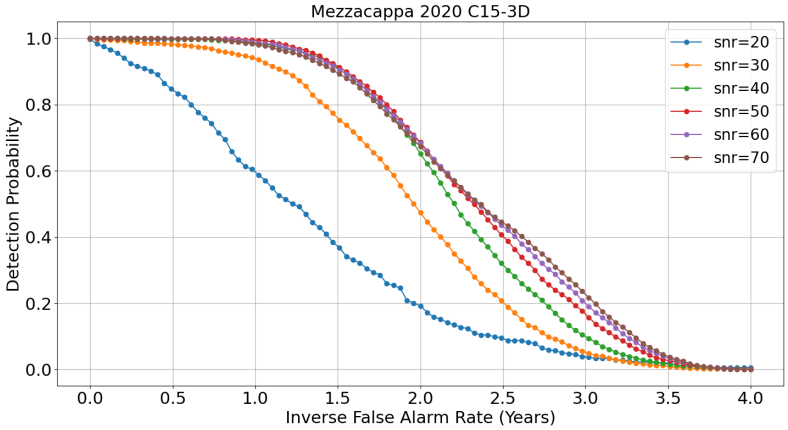

Figure 5.9: Above is the receiver operating curve curve for Mezzacappa C15-3D. As stated in previous plots, the 50% probability is met for the higher iFAR values.

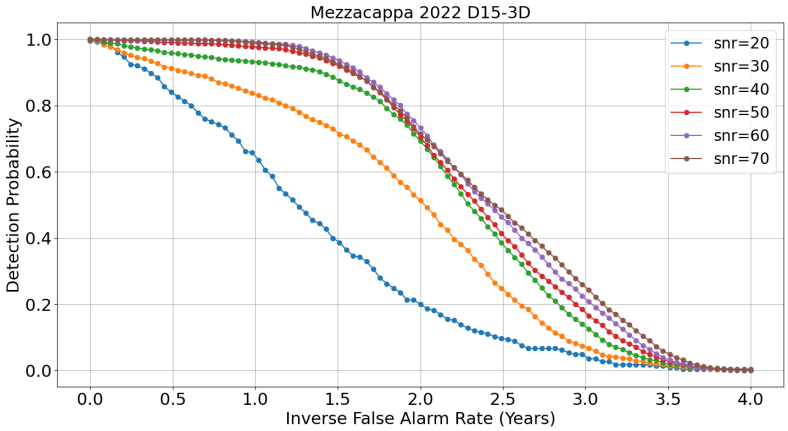

Figure 5.10: Above is the receiver operating curve for Mezzacappa D15-3D. As is the case for the prevous iFAR vs. Detection Probability

CHAPTER VI

DISCUSSION AND FUTURE DIRECTIONS

6.1 Discussion

6.1.1 Overall pipeline performance

The 50% efficiencies of all of the waveforms analyzed by cWB and MuLaSEcC are presented in figures 5.1 and 5.2 respectively, and the 50% efficiencies for MuLaSEcC themselves are listed below in table 6.1.

Table 6.1: The table above shows the names of each of the waveforms, and a brief description of their major features, with a greater detail of each given in table 3.2, and then the efficiency curve SNR for each at 50% efficiency.

Waveform name	Model description	SNR at 50\% efficiency
s20	20 solar mass 3D model	25
s27	27 solar mass 3D model	35
s15nr	15 solar mass, non rotating 3D model	25
s15fr	15 solar mass, fast rotating 3D model	15
s15r	15 solar mass, rotating 3D model	25
fiducial	35 solar mass, fast rotating 2D model	25
TM1	15 solar mass, non rotating 3D model	20
SFHx	15 solar mass, non rotating 3D model	15
C15-3D	15 solar mass, non rotating 3D model	35
D15-3D	15 solar mass, non rotating 3D model	35
mesa20	20 solar mass, non rotating 3D model	25
s18	18 solar mass, non rotating 3D model	30
m39	39 solar mass, non rotating 3D model	20
s9	09 solar mass, non rotating 3D model	15
s13	13 solar mass, non rotating 3D model	15
A300w0.50_HSDD2	12 solar mass, slowly rotating 2D model	15

From table 6.1, we can see the 50% efficiency ranges from SNR 15 - SNR 35.

We can conclude that MuLaSEcC preforms better for s15fr, SFHx, s9, s13, and A300w0.50_HSDD2.

We further examined 4 waveforms in more detail and compaired their efficiencies as a function of SNR with the same for the cWB pipeline efficiencies. These are the Mezzacappa C15-3D [15] and D15-3D [14] models, Cedra Duran fiducial [7], and the Kuroda TM1 model [13]. A brief description of each of these models is given in table 6.1 above. We have found that the MuLaSEcC pipeline performs more efficiently for the Cerda Duran fiducial and Kuroda TM1 pipelines for this range of data when the SN2019ejj happened. It may be noted that D15 is one of the most recent CCSN waveforms that has been published. One can train the CNN more carefully with incorporation of these newer waveforms to improve the efficiency for MuLaSEcC.

It may be noted that figures 5.1 to 5.6, which represent the detection probability (DP) of selected waveforms as a function of the SNR, have been plotted in the OSW of SN2019ejj, where the interferometer noise had been changing, i.e., non-stationary, and hence the false alarm rate (FAR) had also been changing. However, for a proper comparison of pipeline performance, one should evaluate DP at a fixed value of false alarm. Thus, these plots can be seen to only represent fractions of signals recovered for each injection simulation at fixed SNR for each of these pipelines, but their performances can not be deduced from this plot alone. To compare efficiencies at fixed FAR, both sets of ROC's (MuLaSEcC and cWB) should be created for each SNR value, and then a fixed value of FAR should be chosen, and the DP should be plotted against the corresponding SNR's. This will be shown in a future study.

6.1.2 CNN training

The CNN itself consistently performed well and accurately, and consistently correctly classified waveforms from signal, even when analyzing waveforms that the CNN was not trained on.

6.2 Future directions

6.2.1 Active use in O4

The most imminent direction to take this pipeline is to apply it in the currently running fourth observation run of LIGO. This means that if there is a supernova event in LIGO's detectable range, we will run our pipeline on the specific duration.

6.2.2 CNN improvements

One major avenue for us to improve our pipeline is to improve our CNN. There is further work to be done in improving our CNN. We can do this by being more selective in choosing which waveforms we train our CNN on. In this study we choose a set of training waveforms with the intent of having as wide a range of waveforms as possible. But supernova simulators have

pointed out that some of the waveforms that we have trained our network on are either nonphysical (namely 2D simulations) or have been later proven to be outdated. Future work with simulators to choose more realistic simulations and be more selective with them may prove to give better results and more inconsistent results. An example will be to include the Mezzacappa D15 waveform in the training set.

6.2.3 Standalone pipeline

A second major direction to take the pipeline is to eventually develop it into a standalone pipeline. Currently MuLaSEcC exists as a cWB plugin and using LIGO GRID computing and cluster. But as discussed in this thesis, the MuLaSEcC pipeline does not require cWB post-processing, and only used the network analysis. One of the directions in the near future will be to create a network analysis that is independent of the cWB. This will enable the MuLaSEcC to operate in a standalone mode and will not have to keep up with the cWB code versions.

REFERENCES

[1] B. P. ABBOTT AND ET AL., *Observation of gravitational waves from a binary black hole merger*, Phys. Rev. Lett., 116 (2016), p. 061102.

[2] B. P. ABBOTT AND ET AL., *Multi-messenger observations of a binary neutron star merger**, The Astrophysical Journal Letters, 848 (2017), p. L12.

[3] H. ANDRESEN, B. MÜLLER, E. MÜLLER, AND H.-T. JANKA, *Gravitational wave signals from 3D neutrino hydrodynamics simulations of core-collapse supernovae*, Monthly Notices of the Royal Astronomical Society, 468 (2017), pp. 2032–2051.

[4] H. ANDRESEN, E. MÜLLER, H.-T. JANKA, A. SUMMA, K. GILL, AND M. ZANOLIN, *Gravitational waves from 3D core-collapse supernova models: The impact of moderate progenitor rotation*, Monthly Notices of the Royal Astronomical Society, 486 (2019), pp. 2238–2253.

[5] A. BUIKEMA AND ET AL., *Sensitivity and performance of the advanced ligo detectors in the third observing run*, Phys. Rev. D, 102 (2020), p. 062003.

[6] B. W. CARROLL AND D. A. OSTLIE, *An Introduction to Modern Astrophysics*, Cambridge University Press, 2 ed., 2017.

[7] P. CERDÁ-DURÁN, N. DEBRYE, M. A. ALOY, J. A. FONT, AND M. OBERGAULINGER, *Gravitational wave signatures in black hole forming core collapse*, The Astrophysical Journal Letters, 779 (2013), p. L18.

[8] V. COLLABORATION, *The virgo collaboration*, Virgo Technical Report, (2009).

[9] G. M. HARRY AND (FORTHE LIGO SCIENTIFIC COLLABORATION), *Advanced ligo: the next generation of gravitational wave detectors*, Classical and Quantum Gravity, 27 (2010), p. 084006.

[10] KAGRA COLLABORATION AND ET AL., *KAGRA: 2.5 generation interferometric gravitational wave detector*, Nature Astronomy, 3 (2019), pp. 35–40.

[11] S. KLIMENKO, I. YAKUSHIN, A. MERCER, AND G. MITSELMAKHER, *A coherent method for detection of gravitational wave bursts*, Classical and Quantum Gravity, 25 (2008), p. 114029.

[12] W. KUNKEL, B. MADORE, I. SHELTON, O. DUHALDE, F. M. BATESON, A. JONES, B. MORENO, S. WALKER, G. GARRADD, B. WARNER, AND J. MENZIES, *Supernova 1987A in the Large Magellanic Cloud*, , 4316 (1987), p. 1.

[13] T. KURODA, K. KOTAKE, AND T. TAKIWAKI, *A new gravitational-wave signature from standing accretion shock instability in supernovae*, The Astrophysical Journal Letters, 829 (2016), p. L14.

[14] A. MEZZACAPPA, P. MARRONETTI, R. E. LANDFIELD, E. J. LENTZ, R. D. MURPHY, W. RAPHAEL HIX, J. A. HARRIS, S. W. BRUENN, J. M. BLONDIN, O. E. BRONSON MESSER, J. CASANOVA, AND L. L. KRONZER, *Core collapse supernova gravitational wave emission for progenitors of 9.6, 15, and* $25\mathrm{m}_{\odot}$, Phys. Rev. D, 107 (2023), p. 043008.

[15] A. MEZZACAPPA, P. MARRONETTI, R. E. LANDFIELD, E. J. LENTZ, K. N. YAKUNIN, S. W. BRUENN, W. R. HIX, O. E. B. MESSER, E. ENDEVE, J. M. BLONDIN, AND J. A. HARRIS, *Gravitational-wave signal of a core-collapse supernova explosion of a* $15\ M_{\odot}$ *star*, Phys. Rev. D, 102 (2020), p. 023027.

[16] V. MOROZOVA, D. RADICE, A. BURROWS, AND D. VARTANYAN, *The gravitational wave signal from core-collapse supernovae*, The Astrophysical Journal, 861 (2018), p. 10.

[17] S. MUKHERJEE, G. NURBEK, AND O. VALDEZ, *Study of efficient methods of detection and reconstruction of gravitational waves from nonrotating 3d general relativistic core collapse supernovae explosion using multilayer signal estimation method*, Phys. Rev. D, 103 (2021), p. 103008.

[18] S. MUKHERJEE, L. SALAZAR, J. MITTELSTAEDT, AND O. VALDEZ, *New method for enhanced efficiency in detection of gravitational waves from supernovae using coherent network of detectors*, Phys. Rev. D, 96 (2017), p. 104033.

[19] E. P. O'CONNOR AND S. M. COUCH, *Exploring fundamentally three-dimensional phenomena in high-fidelity simulations of core-collapse supernovae*, The Astrophysical Journal, 865 (2018), p. 81.

[20] J. POWELL AND B. MÜLLER, *Gravitational wave emission from 3D explosion models of core-collapse supernovae with low and normal explosion energies*, Monthly Notices of the Royal Astronomical Society, 487 (2019), pp. 1178–1190.

[21] ——, *Three-dimensional core-collapse supernova simulations of massive and rotating progenitors*, Monthly Notices of the Royal Astronomical Society, 494 (2020), pp. 4665–4675.

[22] D. RADICE, V. MOROZOVA, A. BURROWS, D. VARTANYAN, AND H. NAGAKURA, *Characterizing the gravitational wave signal from core-collapse supernovae*, The Astrophysical Journal Letters, 876 (2019), p. L9.

[23] M. J. SZCZEPAŃCZYK, J. M. ANTELIS, M. BENJAMIN, M. CAVAGLIÀ, D. GONDEK-ROSIŃSKA, T. HANSEN, S. KLIMENKO, M. D. MORALES, C. MORENO, S. MUKHERJEE, G. NURBEK, J. POWELL, N. SINGH, S. SITMUKHAMBETOV, P. SZEWCZYK, O. VALDEZ, G. VEDOVATO, J. WESTHOUSE, M. ZANOLIN, AND Y. ZHENG, *Detecting and reconstructing gravitational waves from the next galactic core-collapse supernova in the advanced detector era*, Phys. Rev. D, 104 (2021), p. 102002.

[24] M. J. SZCZEPACZYK, *Multimessenger Astronomy with Gravitational Waves from Core-Collapse Supernovae*, PhD thesis, Nov 2019.

[25] M. J. SZCZEPAŃCZYK, Y. ZHENG, J. M. ANTELIS, M. BENJAMIN, M.-A. BIZOUARD, A. CASALLAS-LAGOS, P. CERDÁ-DURÁN, D. DAVIS, D. GONDEK-ROSIŃSKA, S. KLIMENKO, C. MORENO, M. OBERGAULINGER, J. POWELL, D. RAMIREZ, B. RATTO, C. RICHARSON, A. RIJAL, A. L. STUVER, P. SZEWCZYK, G. VEDOVATO, M. ZANOLIN, I. BARTOS, S. BHAUMIK, T. BULIK, M. DRAGO, J. A. FONT, F. D. COLLE, J. GARCÍA-BELLIDO, V. GAYATHRI, B. HUGHEY, G. MITSELMAKHER, T. MISHRA, S. MUKHERJEE, Q. L. NGUYEN, M. L. CHAN, I. D. PALMA, B. J. PIOTRZKOWSKI, AND N. SINGH, *An optically targeted search for gravitational waves emitted by core-collapse supernovae during the third observing run of advanced ligo and advanced virgo*, 2023.

BIOGRAPHICAL SKETCH

Michael Benjamin obtained his Bachelors degree in Space Physics in 2021 at Embry Riddle Aeronautical University in Prescott Arizona with a minor in Mathematics. While at Embry Riddle, he joined the Laser Interferometer Gravitational wave Observatory (LIGO) national collaboration. In the summer of 2019 he was accepted for a summer internship at the Research Experience for Undergraduates (REU) at the University of Texas Rio Grande Valley and presented a poster showcasing his summer research. He then presented a poster at the American Physics Society (APS) 4-corners meeting in October 2019. He then presented the following year at the APS 4-corners meeting in October 2020. After graduating, he was accepted for the Master's in Physics program at the University of Texas Rio Grande Valley (UTRGV). While at UTRGV, he presented numerous times, twice at the UTRGV College of Science colloqium, Twice at the LIGO-VIRGO-KAGRA (LVK) collaboration, and then presented at the October 2022 APS Texas section conference. Michael Benjamin has earned his Master's in Physics from University of Texas Rio Grande, graduating in July 2023. Michael Benjamin can be reached at his personal email, michael.benjamin104@gmail.com.